Effect of annealing temperature on the physical properties of NiO thin films and ITO/NiO/Al Schottky diodes

Parashurama Salunkhe[1] and Dhananjaya Kekuda[1,*]

[1] *Department of Physics, Manipal Institute of Technology, Manipal Academy of Higher Education, Manipal 576104, India*

ABSTRACT

Herein, fabrication and characterisation of p-NiO/Al Schottky barrier diodes have been realised by dc reactive magnetron sputtering. In addition, effect of post-annealing temperature was studied. A detailed investigation on the physical properties of the NiO thin films was carried out using structural, morphological, optical, and spectroscopic characterisation tools. The metal–semiconductor interface behaviour has been analysed by current–voltage characterisation by implementing the Thermionic emission and Chueng model. The fabricated diode rectification ratio of 10^3 has been recorded at $\pm 3V$, and barrier height varied from 0.53 to 1.10 eV as a function of annealed treatment. A space charge-limited conduction mechanism and tunnelling through the interface trap density of p-NiO/Al Schottky diodes were explained by power law characteristics. Furthermore, we have evaluated the Schottky device's electrical characteristics through the ac measurements which include capacitance densities, dielectric constants, tangent loss, AC conductivity, and Nyquist plots. The present work could provide a better understanding and insight into the p-NiO/Al Schottky junction.

1 Introduction

In recent years, oxide semiconductors and transition metal oxides are attracted very much towards transparent micro-/nanoelectronics applications owing to their inherent physical properties. Interestingly, oxide semiconductors are optically transparent in the visible region with tuneable bandgap and electrical conductivity. Moreover, these are chemically stable and mechanically durable for device fabrication. Understanding the physical properties of oxide semiconductors such as electrical, optical, and chemical composition is essential so that they are beneficial for device applications. Specifically, the characteristics of metal–semiconductor junction (M-S) and heterojunctions need to be investigated to meet applications in science and technology. Oxide semiconductors are having great potential

Address correspondence to E-mail: dhaya.kekuda@manipal.edu

advantages over conventional semiconductors such as Si, Ge, etc. because of their superior physical properties which can be easily tuned by varying the processing parameters. Some of the oxide semiconductors such as zinc oxide (ZnO), titanium oxide (TiO_2), indium-doped tin oxide (ITO), fluorine-doped tin oxide (FTO), nickel oxide (NiO), etc. exhibit desirable properties depending upon the processing parameters [1–4]. They can be used in variety of applications which include integrated circuits, photovoltaic cells, sensors, thin film transistors (TFTs), photodetectors, field-effect transistors (FETs), heterojunction bipolar transistors, etc. [5–10].

In recent years, nickel oxide (NiO) material has attained much interest in electronic, photonics, and optoelectronic applications owing to its performance. NiO thin film exhibits intrinsically p-type conductivity, and it is a promising material for UV photodetector due to its wide range of optical bandgap ∼ 3.3 to 3.5 eV [11, 12]. Moreover, it has lower electron affinity ranging from 1.46 to 1.85 eV and it is abundant in the earth's crust and stable in severe environmental circumstances [13]. In addition, it exhibits a crystal structure of face centre cubic nature, in which Ni vacancies and oxygen interstitials are arranged in a cubic close-packed lattice with an octahedral void, similar to NaCl type crystal structure [12]. The resistivity of the NiO thin films can be tuned by creating intrinsic defects as Ni^{3+} resulting in a lowering of the resistivity. In addition, doping conducting materials such as Ag, Cu, Li, etc. may enhance the conductivity of the film [14]. The previously reported literature on n-type NiO thin films includes the tuning of deposition parameters, especially varying oxygen partial pressures that can be used for homojunction applications [11, 15, 16].

In the electronics sector, the metal–semiconductor (MS) contact is one of the most extensively utilised rectifying contacts [17]. Schottky diodes, the most basic of the MS contact devices, are of great technological importance; thus, a comprehensive study of their electrical characteristics is of major interest. Besides, the mechanism of current flow through the interface is still to be elucidated, and the exact value of the barrier height is yet to be evaluated using current–voltage (I–V) characteristics. Moreover, impedance characteristics on p-NiO/Al Schottky diode are not explored in detail till date [18, 19]. In this present work, we have fabricated and characterised the ITO/p-NiO/ Al Schottky diodes and investigated physical properties as a function of post-annealing treatment of the sputtered p-NiO thin film. To the best of our knowledge, a detailed report on p-NiO/Al Schottky diode was realised by dc reactive magnetron sputtering with photo response studies.

2 Experimental details and characterisation

The ITO substrates were cleaned by standard RCA procedure, and substrates were exposed to the UV-ozone treatment for about 10 min. NiO thin films were deposited by reactive magnetron sputtering using a metallic Ni target (Ni—99.99%) of 2 inch diameter and oxygen (purity—99.999%) as a reactive gas. In the overall deposition process, sputter gas as argon acts very crucially, and it can be controlled by using a standard mass flow controller (Alicat Scientific, Inc. MFC). In addition, oxygen flow rate, sputter power, substrate heater, etc. also play a major role in getting the desired film. As-deposited samples were post-annealed for an hour to enhance the crystallinity of the film in the temperature range of 100 to 400 °C. To confirm the structural properties, a grazing angle x-ray diffractometer (XRD) was used. Chemical composition and the oxidation state were determined by x-ray photoelectron spectroscopy (XPS). Surface morphology was analysed by atomic force microscopy (AFM). Optical characterisation was carried out by Shimadzu 1800 UV–Visible spectrophotometer. For fabrication of the Schottky diode, samples were coated with aluminium metal electrodes using a shadow mask by using a thermal evaporation unit. The thickness of the metal electrode was fixed at 80 nm, and the evaporation rate was maintained at 5 $Ås^{-1}$. Finally, all Schottky diodes were characterised by using current–voltage and impedance studies through a Keithley 4200 SCS semiconductor characterisation unit. A schematic illustration of the device structure is shown in Fig. 1. The energy band diagram of the NiO/Al junction is depicted in Fig. 2.

3 Results and discussion

The X-ray diffraction pattern of the NiO thin films is depicted in Fig. 3a. Grown all films exhibited polycrystalline nature on the ITO glass substrates. It can

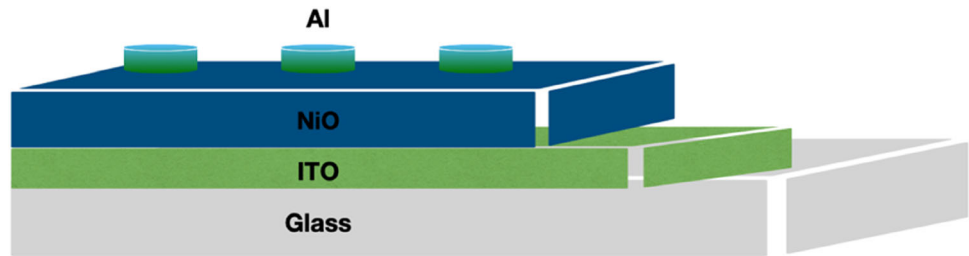**Fig. 1** Structural illustration of the Schottky diode

Fig. 2 Schematic energy band alignment of the Schottky diode
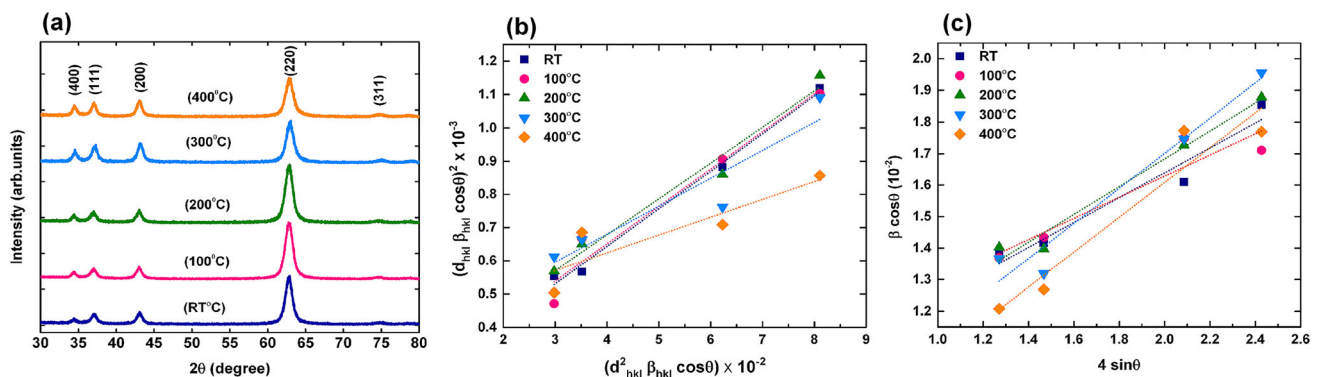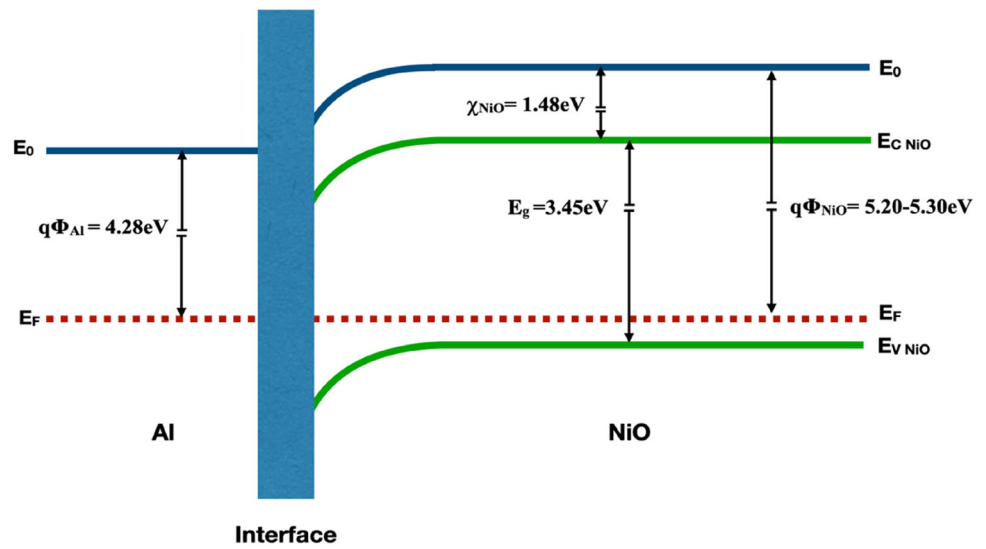

Fig. 3 **a** Grazing angle X-ray diffraction (GXRD) patterns of the NiO thin films deposited on ITO substrates and processed different post-annealing treatment **b** Williamson–Hall (WH) plot **c** Size–strain (SS) plot

be observed that (220) preferred orientation plane is followed by(111),(200), and (311) Braggs peaks are located at 2θ angles of 62.84°,37.04°,43.04°,74.72°, respectively [20]. In addition, ITO substrates Bragg reflection peak (400) also presented in the XRD spectra at 34.40° [21]. Basically, the properties of the NiO film primarily rely on the composition of Ar/O_2 gas mixture and applied sputter power in the reactive sputtering method. Moreover, external thermal

treatment plays a vital role in establishing a better quality of the crystalline film. As the post-annealing temperature increased from room temperature to 400°C, full-width half maxima (FWHM) peak values have decreased and individual peak intensity has significantly increased. Such kind of behaviour indicates that high crystallinity is induced in the film due to the post-annealing process. The grown NiO thin film crystallographic arrangement has a typical NaCl

face-centred cubic (FCC) structure and their crystal structure strongly depended on Ni^{2+} and O^{2-} ions. To compute the crystallite size and confirm the possible strains present in the films, we have plotted the Williamson-Hall plot, which is depicted in Fig. 3b.

$$\beta_{hkl}\cos\theta = \frac{K\lambda}{D} + 4\varepsilon\sin\theta \qquad (1)$$

$$\varepsilon = \frac{\beta\cos\theta}{4\sin\theta} \qquad (2)$$

In addition, we have applied a size–strain plot to estimate the crystallite size and presence of strain in the film by using the following equations,

$$\beta_{hkl} = \beta_L + \beta_G \qquad (3)$$

where β_L broadening due to Lorentzian function and β_G broadening due to Gaussian function

$$(d_{hkl}\beta_{hkl}\cos\theta/\lambda)^2 = k/D\left(d_{hkl}^2\beta_{hkl}\cos\theta/\lambda\right) + (2\epsilon)^2 \qquad (4)$$

where $d = \sqrt{\frac{a^2}{h^2+k^2+l^2}}$ and k is the shape factor

The size–strain plot of $(d_{hkl}\beta_{hkl}\cos\theta)^2$ versus $(d_{hkl}^2\beta_{hkl}\cos\theta)$ for 2θ values ranging from 30° to 80° is shown in Fig. 3c. Computed crystallite size from the slope of the fitted line and strain can be estimated from the square root of the y-intercept [22]. We have estimated the lattice parameters of NiO films and it was marginally reduced from 4.19 Å to 4.18 Å due to thermal annealing. Post-annealing procedure implies better crystallinity with a low dislocation density of the atoms in the NiO film. Estimated lattice parameters, dislocation density, and other structural properties are listed in Table 1. The adatoms gain additional kinetic energy and deposit Ni^{2+} and O^{2-} ions rearrange on the substrate to form the desired crystalline structure after post-annealing treatment [23, 24].

The AFM images of NiO thin films are depicted in Fig. 4. The study was carried out in a tapping mode to analyse the surface morphology of the samples. From the images, it is clear that uniformly distributed grains and smooth surfaces are evident in the film. Sputtered NiO film's surface features show distinct nanocrystalline grains and grain boundaries and roughness ranging from 7.35 nm to 9.08 nm. The average roughness was 7.35 nm and was recorded in the selected 2×2 μm^2 area of the room temperature processed film. As we increased the annealing temperature, the crystallinity of the film significantly improved. The enhanced crystallinity is believed to

Table 1 Physical properties of NiO thin films deposited on ITO substrate at different annealing temperatures

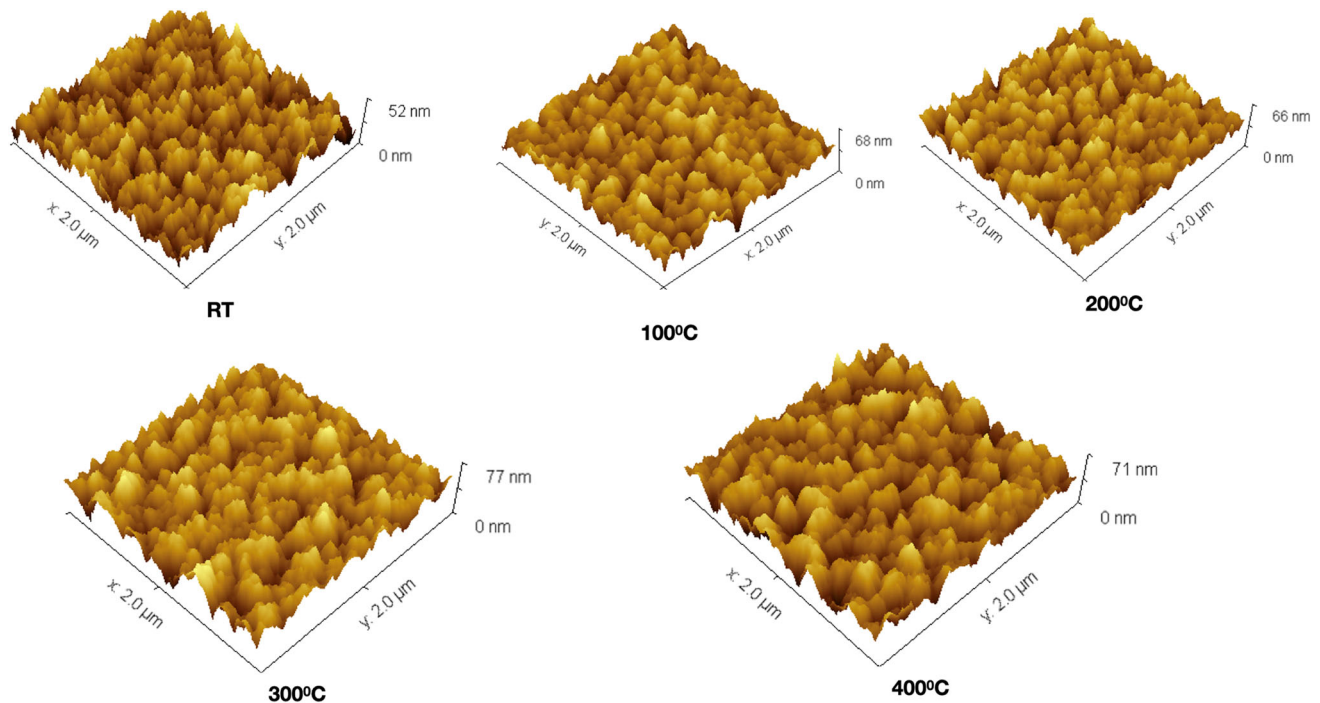| Sample code	Annealing temperature (°C)	W–H plot Crystallite size (nm)	W–H plot Strain (10⁻³)	S–S plot Crystallite size(nm)	S–S plot Strain (10⁻³)	Lattice parameter 10⁻¹⁰ NiO	Lattice parameter 10⁻¹⁰ ITO	Dislocation density/m² 10⁻¹⁶	Crystallites per unit area/m² 10¹⁷	Roughness (nm) (average)	NiO Band gap (eV)
K1	RT	17.05	8.49	12.80	13.80	4.19	10.41	1.23	2.80	7.35	3.11
K2	100	15.13	3.36	12.86	14.16	4.19	10.42	1.22	2.86	7.59	3.39
K3	200	18.10	8.00	13.39	15.67	4.19	10.41	1.28	2.96	8.15	3.33
K6	300	24.67	5.87	17.19	20.24	4.19	10.39	1.30	3.15	8.68	3.23
K9	400	28.84	5.02	27.01	18.52	4.18	10.37	1.19	2.71	9.08	3.15

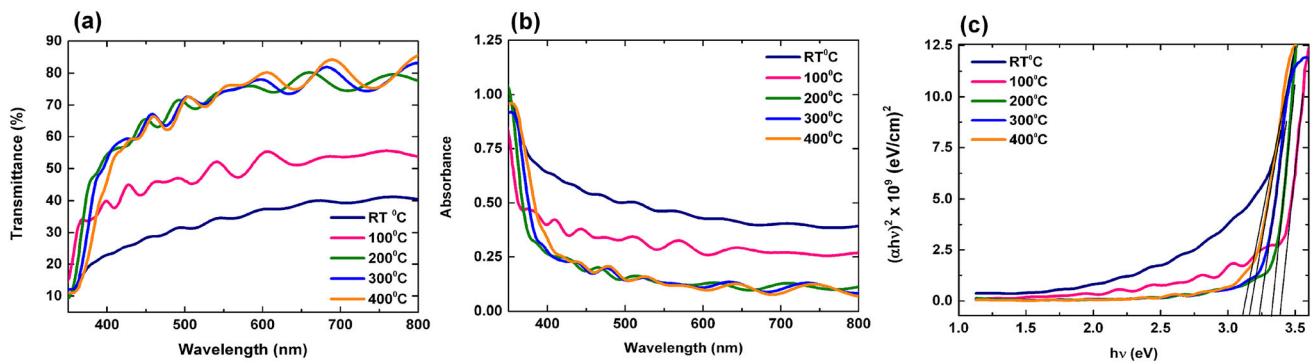**Fig. 4** AFM images of NiO thin films at different post-annealing temperatures

Fig. 5 a Transmission spectra **b** Absorption spectra **c** Tauc plot of the NiO films

be due to extra energy supplied to the film in terms of the temperature and it could cause reduced defects. However, the presence of bigger grains with reduced grain boundaries can cause favourable charge transport in the devices.

We have investigated the optical transmittance spectra of NiO thin films deposited on ITO-coated glass substrates at various annealed temperatures. Figure 5a, b represents the sharp edges in the spectra with semi-transmittance in the visible region $(400 - 700 nm)$. The as-deposited NiO thin films have shown a transmittance of $\sim 37.50\%$ in the visible domain. With an increasing annealing temperature to $100°C$, the transmittance of the film markedly

increased to 55%. Further increasing the annealing temperature to 300 °C and 400°C, the transmittance increased to 80.30%. It can be observed that annealed samples with increased surface roughness and crystallinity resulted in better transmittance. As-deposited NiO thin films contain more intrinsic defects that are Ni^{3+} ions, which tend to cause lower transmittance and smaller energy bandgap. Moreover, the presence of intrinsic defects such as Ni vacancies and Oxygen interstitials absorbs more light causing poor transmittance in the as-deposited films [16].

In addition, the presence of Ni^{3+} ions enhanced the conductivity of the films. Meanwhile, with increasing annealing temperature, it was observed that

transmittance of the film also increased and there is a marginal increase in the energy gap for the films annealed at 100 °C as shown in Fig. 5c. Further increase in the annealing temperature in the range 200–400 °C has resulted in an increase in nanocrystalline size and it was caused by a narrowing of the optical bandgap. Overall, the NiO film optical band gap has reduced from 3.34 to 3.14 eV. For

optoelectronic device applications where tuneable transmittance and electrical properties are required, such films can be utilised.

X-ray photoelectron spectroscopy (XPS) measurements were carried out to confirm the chemical composition and oxidation state of NiO thin film. Figure 6 depicts elemental mapping carried out over a range of 0 to 1200 eV in the XPS wide spectra, in which there were no impurity peaks appeared. It consists of photoemission peaks such as Ni3s, Ni3p, O1s, C1s, and Ni2p, along with Auger electron peaks Ni LMM, O KLL peaks were identified [16]. Before analysing the spectra, the standard carbon correction was set at 284.8 eV to survey spectra, Ni2p and O1s spectra. Figure 7a, b presents XPS $Ni2p_{3/2}$ spectrum applied with Shirley type of background, and various peaks were identified using deconvolution method by Gaussian–Lorentzian mode. In this case, we have observed that 853.77—853.80 eV pertains to Ni^{2+} and it represents the nickel–oxygen bonding along with the face-centred cubic alignment of the crystal structure [25]. Subsequently, another peak was noticed at 855.46–855.56 eV corresponding to Ni^{3+} state, which is ascribed to nickel vacancies [26]. In addition, a broad satellite peak has been identified, which
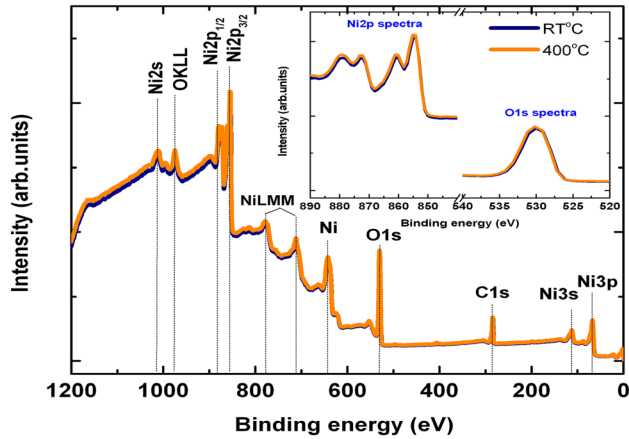

Fig. 6 XPS survey spectra of sputtered NiO thin films on ITO substrates. Blue colour: room temperature and orange colour: 400 °C annealed film

Fig. 7 NiO thin films XPS spectra. **a** and **b** XPS spectra representing core level $Ni2p_{3/2}$. **c** and **d** O1s core level spectra. Measured results black line: original spectra, Navy blue line: fitted spectra, Dark green line: Shirley type background
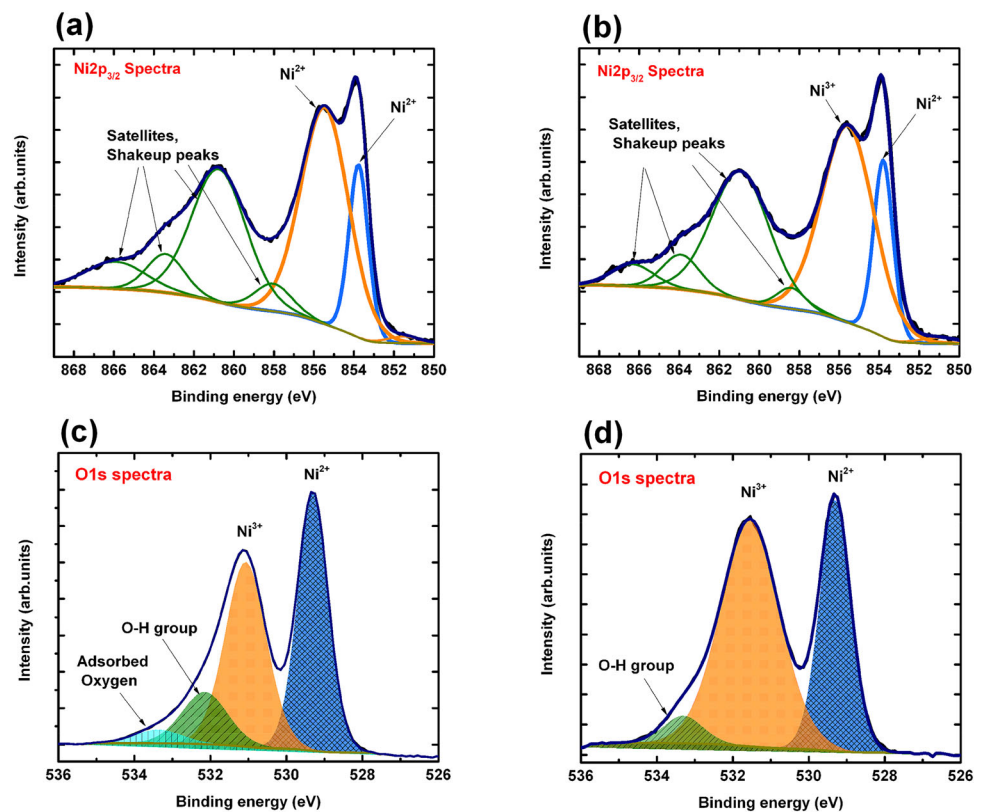
**Table 2** XPS Ni2p atomic composition at room temperature and 400°C annealed samples

Temperature (°C)	Binding energy (eV)	FWHM (eV)	Atomic (%)	Peak assignment	Binding Energy (eV)	FWHM (eV)	Atomic (%)	Peak assignment
Room temperature	851.50	1.86	0.84	Ni^0	529.30	0.94	42.80	Ni^{2+}
	853.77	1.14	13.27	Ni^{+2}	531.07	1.26	40.95	Ni^{3+}
	855.46	2.81	41.08	Ni^{+3}	532.15	1.41	12.83	O–H
	858.04	2.14	3.97	Satellite, shakeup	533.37	1.46	3.42	Adsorbed oxygen
	860.75	3.22	28.76	Satellite, shakeup				
	863.41	2.20	5.71	Satellite, shakeup				
	865.90	3.50	6.37	Satellite, shakeup				
400 °C	850.97	2.29	0.90	Ni^0	529.30	0.95	35.02	Ni^{2+}
	853.80	1.13	14.18	Ni^{+2}	531.55	1.82	60.21	Ni^{3+}
	855.56	3.08	42.73	Ni^{+3}	533.30	1.19	4.77	Adsorbed oxygen
	858.40	1.67	2.47	Satellite, shakeup				
	860.92	3.41	30.61	Satellite, shakeup				
	863.91	2.17	5.28	Satellite, shakeup				
	866.33	2.49	2.47	Satellite, shakeup				

presents the shake-up process. In Fig. 7c, d, O1s spectra show three peaks, in which peak intensity at 529.30 eV reveals that Ni–O interaction again confirms octahedral void space with cubic structure. The peak at 531.07 eV to 531.55 eV is ascribed to the nickel vacancies and oxygen interstitials or Ni^{3+} state induced on the surface of the film [24, 27]. Besides, a tiny peak at 532.15 eV represents the O–H group on the surface of the film and another peak at ∼ 533.30 eV stands for adsorbed oxygen content present on the film surface.

It is evident that under post-annealing treatment, the area under the curve of the Ni^{3+} the state has significantly increased from 40.95 to 60.21% which is evident from the O1s XPS spectra. Therefore, here we have concluded that post-annealing temperature creates more nickel vacancies and oxygen interstitials which are predominantly responsible for p-type conductivity in the films. Furthermore, from the $Ni2p_{3/2}$ and O1s spectra, the ratio of Ni^{3+}/Ni^{2+} considerably increased from 0.95 to 1.17 due to the post-annealing. Hence, in sputtered NiO films annealed at a higher temperature, Ni^{2+} states are ionised and get transformed into Ni^{3+}. Meanwhile, the post-annealing treatment effectively reduced the unwanted O–H and adsorbed oxygen content present on the film surface. The XPS Ni2p and O1s spectrum detailed chemical composition is listed in Table 2.

There is a small chemical shift observed in the Ni2p spectra, which is also reflected in the O1s spectra. It may be due to the binding energy charging effect, which means changes or variations in ionic charge peaks due to changes in their broadening and their chemical concentration due to cation vacancy induced by the oxygen [27]. The increment of the Ni^{3+} ions is due to induced nickel vacancies on the surface of the film and causing p-type characteristics. The following Kroger–Vink notation shows the created Ni vacancies when two neighbouring Ni^{2+} ions get ionised into Ni^{3+} ions by donating an extra electron to oxygen.

$$2\text{Ni}_{Ni}^{x} + \frac{1}{2}\text{O}_2 \rightarrow 2\text{Ni}_{Ni}' + \text{O}_0^x + V_{Ni}' \tag{5}$$
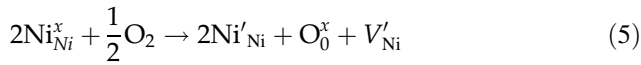
where Ni_{Ni}^{x}, Ni_{Ni}', V_{Ni}', O_o^x stands for Ni^{2+}, Ni^{3+}, the ionised Nickel vacancy and O^{2-} ions, respectively.

Figure 8 depicts the $I - V$ plot and power law characteristics of the NiO/Al Schottky diode measured at room temperature under dark mode. The bias voltage of the device varied from − 3 to 4 V. The characteristics of the $I - V$ curve defined a promising rectification behaviour as observed from the forward and reverse sweeps. In order to fabricate a Schottky diode, on a p-type semiconductor, choosing a lower work function material is desired, and hence, in the present work we have selected aluminium because of

Fig. 8 I-V characteristics of p-NiO/Al Schottky diode measured at room temperature
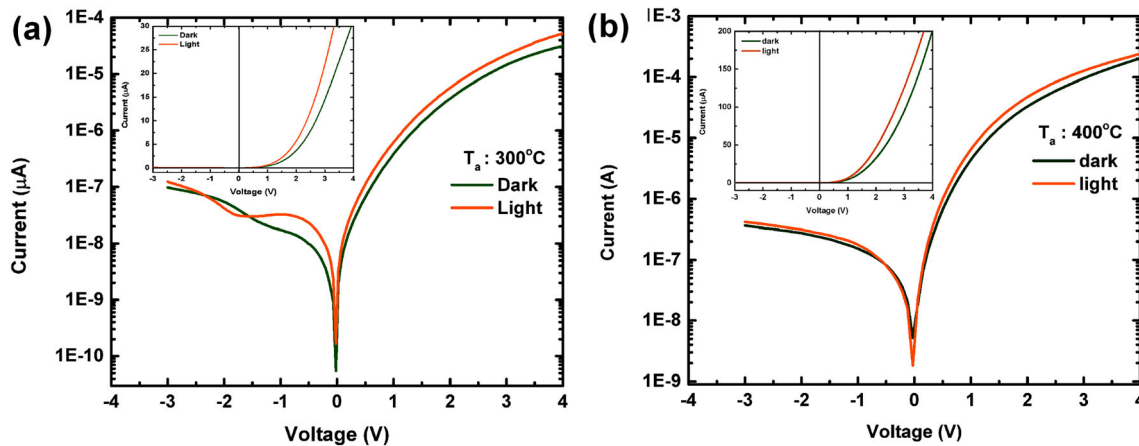
its work function ∼ 4.28 eV. The schematic diagram of the Schottky diode structure is shown in Fig. 1. The $I - V$ characteristics of the constructed Schottky diode were measured at room temperature. A signature of any rectifying junction is the exponential increase in the forward current and week dependence in the reverse voltages, and such a rectifying behaviour was observed in the present study as shown in Fig. 9. The junctions were analysed for the NiO thin films annealed at different temperatures. The rectification behaviour is due to the formation of intrinsic defects in the NiO thin films and the interface between the metal and semiconductor. The ratio of forward to reverse saturation current is ∼ 10^3, for all the devices under dark and illumination. The limited number of charge carriers participates in the formation of metal–NiO interface. At low forward bias voltage–current density drastically rises due to the lowering of energy bands, and a space charge limited current (SCLC) mechanism prevailed [19]. The variation in Schottky diode characteristics depends on many factors such as interfaces, sputtering parameters, the stoichiometry of nickel, and oxygen composition. We have extracted heterojunction parameters such as saturation current, ideal factor (η), and barrier height (Φ_B) from the $I - V$ graph by thermionic emission model (TE).

$$I = I_s\left[\exp\left(\frac{qV}{\eta kT}\right) - 1\right] \tag{6}$$

where, $I_s = AA^*T^2\exp\left(-\frac{q\Phi_B}{kT}\right)$ \tag{7}

I_s is the reverse saturation current, A is the area of the Schottky diode, A^* is the effective Richardson

Fig. 9 $I - V$ characteristics of p-NiO/Al Schottky diode under dark and light mode, **a** 300 °C and **b** 400 °C post-annealed NiO films

Table 3 Comparison of the Schottky diode parameters with the Thermionic emission and Cheung model

Sample code	Condition	TE model		Cheung model		
		η	V_{bi}(eV)	η	V_{bi}(eV)	R_s K-ohm
K1	Dark	5.12	0.74	6.89	0.31	677.71
K2	Dark	3.92	0.72	3.07	0.68	335.82
K3	Dark	1.90	0.77	3.35	0.67	417.83
K6	Dark	2.76	0.79	2.85	0.77	489.50
K6	Light	1.61	0.81	2.02	1.07	290.00
K9	Dark	2.79	0.75	2.71	0.70	364.74
K9	Light	1.84	0.76	2.66	0.80	185.37

constant, $A^* = 96 \text{Acm}^{-2}\text{K}^{-2}$, T is the absolute temperature in Kelvin, η is the ideality factor, k is the Boltzmann constant, and Φ_B is the barrier height of the NiO/Al interface.

From Eq. (6), $V > 3kT/q, -1$ has been neglected and the linear logarithm equation was obtained as follows:

$$\ln I = \frac{qV}{\eta kT} + \ln I_s \qquad (8)$$

We have estimated the ideality factor (η) and barrier height (Φ_B) from the slope of the linear region of the forward region and intercept of the semi logarithm plot of I-V, respectively. We have evaluated the barrier height of the p-NiO/Al junction using Eq. (7), and the values are listed in Table 3. The quality of the diode constructed is decided by the value of the ideality factor (η), which is nearly one for an ideal diode. During the fabrication of the device, the composition of the material, thickness, morphology, and interface may strongly affect the leakage current as well as series resistance (R_s). The presence of defects state in the NiO film may alter these values. Generally, in diodes, the I-V characteristics may deviate from the linear curve and it strongly relays on the series resistance which is one of the important parameters for device performance.

$$I = I_s \left[\exp\left(\frac{q(V - IR_s)}{\eta kT}\right) - 1 \right] \qquad (9)$$

Differentiate Eq. (9) with respect to I, which gives

$$\frac{dV}{d(\ln I)} = IR_s + \frac{\eta kT}{q} \qquad (10)$$

The above equation is a form of a straight-line equation. In order to get the slope and intercept, we can plot $dV/d(\ln I)$ verses I which gives the

series resistance (R_s) and ideality factor (η). Similarly, the plot of $H(I)$ versus I will also provide a series resistance (R_s) along with barrier height (Φ_B) as per the following equation.

$$H(I) = IR_s + \eta \Phi_B \qquad (11)$$

where, $\Phi_B = \left[\dfrac{H(I) - I(R_s)}{\eta}\right]$ and $H(I)$

$$= V - \frac{nkT}{q}\left[\ln\left(\frac{I}{AA^*T^2}\right)\right] \qquad (12)$$

Figure 10 depicts plots of $dV/d(\ln I)$ and $H(I)$ versus under dark mode for all the samples. The measured device parameters such as series resistance, ideality factor, barrier height, and rectification ratios are tabulated and compared with the two different models in Table 3. The $I - V$ characteristics of the Schottky diode were recorded for forward bias voltages larger than the turn-on voltage. The recorded Schottky diode rectifying ratio is $\sim 10^3$ which is depicted in Fig. 9. The operational current starts increasing slowly; then, it rapidly increases due to the diffusion current in the Schottky diode. The turn-on voltage shifts from 1.5 to 2 V for the diodes with NiO films annealed at 300 to 400°C in the dark mode. Such behaviour could be due to the increased series resistance (R_s) of NiO thin films. XPS characterisation confirms the amount of Ni^{2+} states which is responsible for the increased turn-on voltage and resistance of the film. Furthermore, the presence of high series resistance and space charge limited current in the films are crucial for device performance. Figure 9 shows the reverse leakage current of the Schottky diodes in the order of $\sim 10^{-7}$A and 10^{-6}A. Increased leakage current by an order in the 400 °C annealed films could be due to the increased concentration of Ni^{3+} states. The Schottky diodes constructed with low temperature annealed active layers exhibited
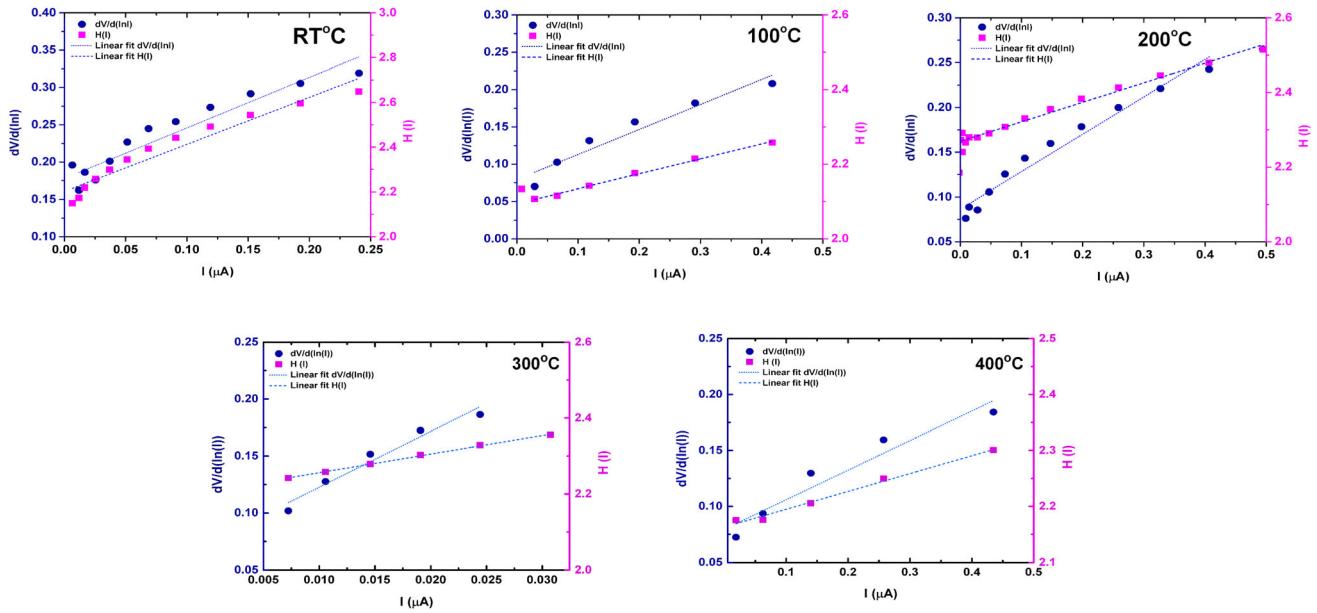
Fig. 10 Representing the dV/d(lnI) and H(I) versus I(A) plots for p-NiO/Al Schottky diode at different annealed temperatures

higher ideality factor with lower Schottky barrier height. In the high temperature annealed samples, the physical and chemical properties were significantly modulated, with a formation of favourable barrier height for the carriers to overcome it, resulting in a decrease in the leakage current and improved ideality factor. Moreover, higher values of the ideality factor suggest a divergence from TE theory by the current mechanism. The estimated ideality factor from both thermionic and Cheung models was greater than unity, and it could be due to the presence of defect traps or interface states in the films. We have also noticed that Schottky barrier height slightly increased from 0.72 eV to 0.81 eV as per the TE model and 0.31 to 0.77 eV as per the Cheung model with increased annealing temperature. We have noticed that at room temperature constructed Schottky diode has a large ideality factor and small barrier height. The XPS deconvoluted O1s spectra show that containing absorbed oxygen elements and the small quantity of O–H groups could be causing the interface between the ITO/p-NiO/Al Schottky diode. In addition, variation in barrier height and ideality factor after post-annealing treatment may be causing the increased surface roughness of the film, chemical composition of the film, interdiffusion of unwanted materials on the film, quantum mechanical tunnelling, image force lowering and presence of a thin insulation layer at the interface [28, 29]. The major discrepancy between the TE model and Cheung model extracted parameters is caused because of the series resistance and presence of defect states (Fig. 11).

Figure 12 depicts the power law characteristics of the NiO/Al Schottky diode measured at room temperature. It is difficult to decide whether the thermionic emission of holes or other transport processes are occurring for a specific voltage range when the junction interface is inhomogeneous. Nevertheless, by analysing the power law characteristics, it is feasible to identify the primary type of transport mechanism for a specific voltage range. The current (I) across the junction varies with the applied voltage (V) as a power m.

$$I \propto V^m$$

where I is the current and m is a slope. As a result, the log I vs. log V plot gives a straight line with a slope of m value. Generally, in the lower voltage region slope values must be unity. Due to dominating thermionic transport mechanism we have found two different regions for the samples. The applied voltage ranges have been divided by a dotted line to mark two regions. In the region I, the slope values varied from 1.12 to 1.82 for all samples. It suggested that the thermionic emission of holes is dominating over the
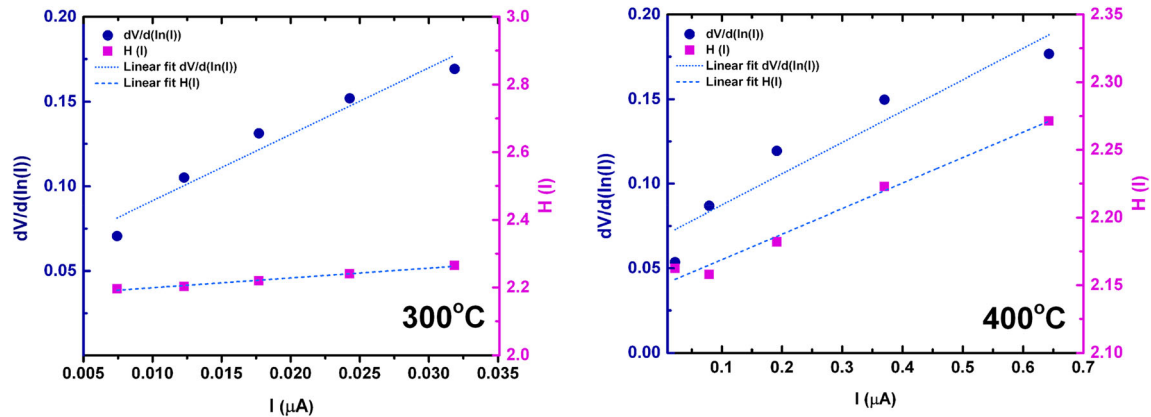
Fig. 11 Representing the $dV/d(\ln I)$ and $H(I)$ versus $I(A)$ plots for p-NiO/Al Schottky diode under light mode
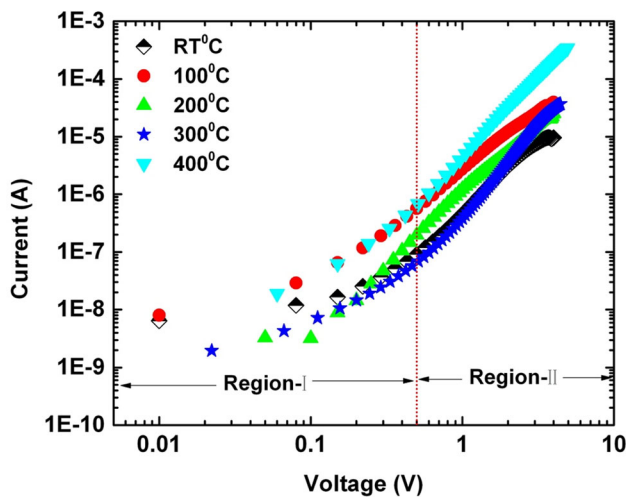

Fig. 12 Power law characteristics of p-NiO/Al Schottky diode measured at room temperature

Schottky barrier height in the transport mechanism [30, 31]. In region II, the obtained slope values greater than 2 that implies a distribution of interface traps or the presence of defects states exist in the NiO/Al junction. It could be causing a small tunnelling contributing at the junction. Moreover, the space charge-limited conduction process prevailed at the junction. Hence, we have concluded that SCLC is dominating over thermionic holes and Schottky barrier height [30, 31]. Therefore, the entire conduction mechanism is due to the barrier inhomogeneity that is diverted from the TE model.

Figure 13a, b shows various post-annealing treatment dependence of the NiO film capacitance density and dielectric permittivity over the range 1 kHz to 1 MHz under room temperature. It can be found that the capacitance of the room temperature processed

and 100 °C post-annealed devices exhibits a significantly decreasing trend with the increasing frequency. Apart from that remaining 200 °C, 300 °C, and 400 °C, processed devices are showing slowly decreasing at the low-frequency range and get stabilised at $\sim 10^5$ to 10^6 Hz. Notably, all processed devices are confirming the capacitance in nano farad ranges and stabilised low capacitance values are indicating that charge carriers are able to respond with the alternating applied field. Such kinds of devices are able to store a low number of charges, and they could be utilised for high-frequency applications [32]. The dielectric permittivity can be measured by following relation $\in = Cd/A\in_0$, where C is the capacitance, d is the thickness of the NiO film, A is the area of the electrode. ϵ_0 is the permittivity of free space. It can be also observed that the dielectric constant of the films has to decrease at a lower frequency and become flat at higher frequency ranges. This is due to as frequency increases it becomes difficult for dipoles to align due to a reduction in the space charge polarisation effect [33]. The frequency dispersion relation with the real part (ϵ') and imaginary part (ϵ'') of the dielectric constant at different annealed samples are shown in Fig. 13c. However, various parameters are involved to decide the dielectric constants of the NiO material such as electronic, ionic orientation, and space charge polarisation. Generally, NiO thin films contain a polycrystalline system; all the charges are piled up when polarisation occurs due to the external electric field applied to the system. Result the decrement of the dielectric permittivity has been observed. Furthermore, the wide energy bandgap and inherent physical properties of the NiO system interfacial
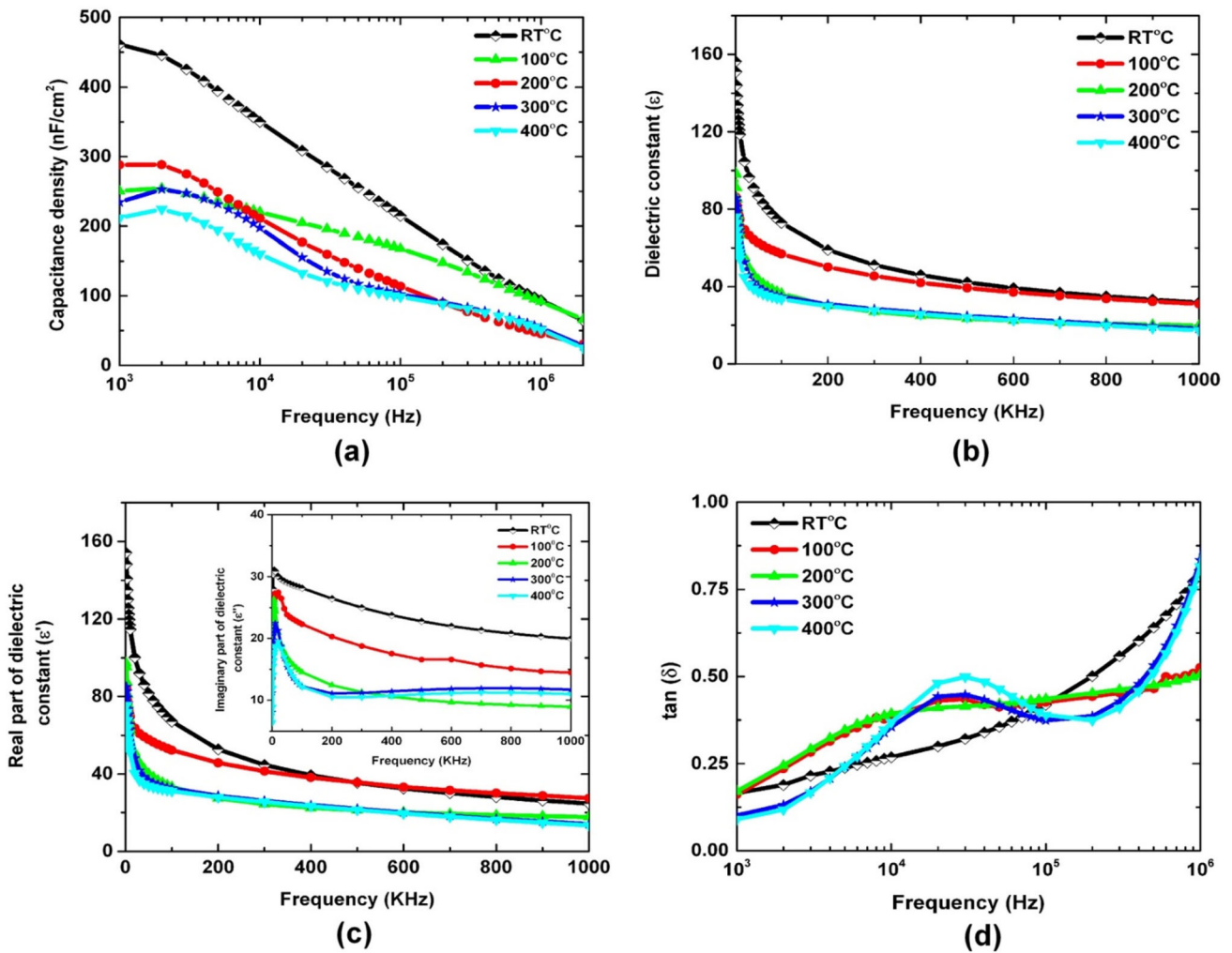
Fig. 13 **a** Frequency vs dependent capacitance density of the device, **b** Dielectric constant vs frequency, **c** Real part of the dielectric constant and inset shows the imaginary part of the dielectric constant vs frequency, **d** Dielectric loss vs frequency of the p-NiO/Al Schottky diode as a function of post-annealing treatment

polarisation cause the higher dielectric permittivity, which consists of an electrically inhomogeneous system and the presence of defects such as Ni^{2+} and Ni^{3+} states.

However, at a higher frequency of the field applied to the film, interfacial charges are not responded to immediately due to the polarised field which was not established. Therefore, at a higher frequency, the obtained dielectric permittivity is stable with frequency. In addition, the grains and grain boundaries extensively contribute to the dielectric permittivity at different frequency regions. Here, it can be noticed that the dielectric constant has been reduced by increasing the post-annealing process. It is reasonable to assume that non-stoichiometry of the NiO films and their defective states are significantly

contributing dielectric constant. In addition, it could be a dominant nature of the interfacial layers between the NiO and its electrodes.

Dielectric loss or tangent loss factor can be defined as the ratio of real and imaginary parts of dielectric constant, i.e. $tan\delta = \in'/\in''$. The dielectric loss occurs because of the absorption of electrical energy which is used to rotate the dipoles in dielectric films. Figure 13d shows the tan δ versus frequency of the post-annealed Al/NiO Schottky diode over the range 1 kHz to 1 MHz characterised under room temperature. We observed two different regions based on the low and high-frequency domains. Decreasing the tangent loss factor is due to the interfacial polarisation at grain boundaries. Similarly in high-frequency regions tangent loss has been attributed to grains.
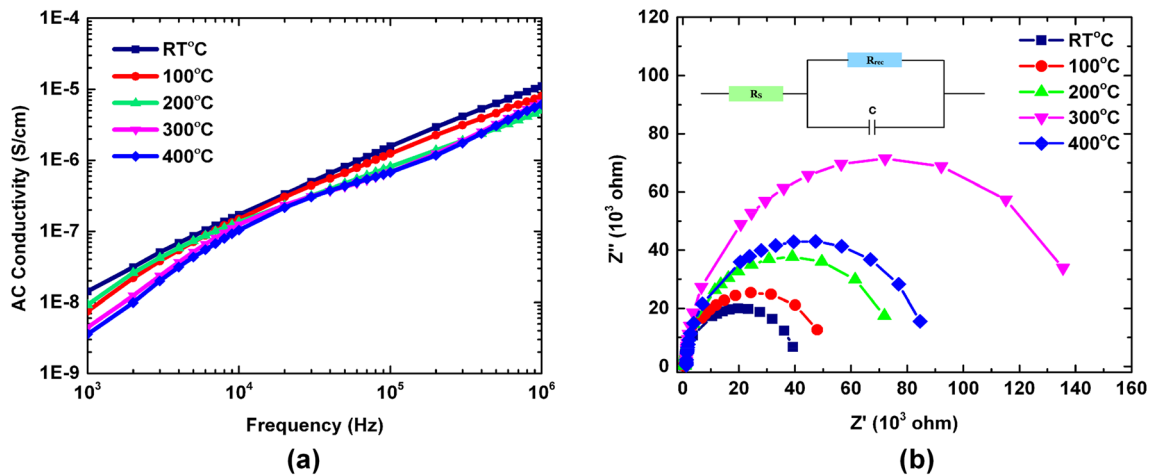
Fig. 14 **a** AC conductivity vs frequency of the studied devices extracted from the measured Impedance data, **b** Nyquist plot at a various annealing temperatures of p-NiO/Al Schottky diode

Generally, in metal oxide thin films in which temperature depended on the fabrication methodology involved, there could be a film homogeneity or the presence of inter defects that can cause the absorption current because the space charge carriers significantly contribute to the dielectric loss [34].

Figure 14a shows the graph of AC conductivity versus frequency characterised at room temperature. To find the ac conductivity of the devices, the following relation is adopted $\sigma_{ac} = \omega\epsilon_0\epsilon'\tan\delta$ where ω is the angular frequency, ϵ_0 is the permittivity of free space, ϵ' is the real part of the dielectric constant. It can be seen that at low frequencies the conductivity has been steady and it has rapidly raised at higher frequencies. In wide band gap materials, especially NiO film has moderate free charge carriers responsible for electrical conduction. Furthermore, the hopping mechanism of bound charges is significantly responsible for the A.C. conductivity. As increasing the applied frequency, these charges are piled up, obtaining a better conductivity.

Figure 14b shows the Nyquist plot of the ITO/NiO/Al Schottky diode performed at room temperature. The real impedance (Z') values versus negative imaginary values (Z'') curves exhibited a single semicircle for all post-annealed devices. Interestingly, the plotted semicircle has shifted towards a lower frequency as we increased the post-annealed temperature of the NiO layer. Generally, semicircle denotes the sum of series resistance and bulk resistance of the fabricated devices. It clearly indicates that the maximum semicircle has significantly increased because

of the grain size contribution. At 300 °C annealed sample, Z' Z'' plot has shown a larger semicircle than the 400 °C, which could be due to the limitation of the ITO back contact and also the high-temperature grain size effect. However, we identify the series resistance which varies from 2.29 K Ω to 5.21 K Ω with respect to room temperature to 400 °C. Hence, we have concluded that fabricated all devices are thermally well activated as a function of post-annealing temperature.

4 Conclusion

In summary, we have fabricated and characterised p-NiO/Al Schottky diode and investigated in detail structural, optical, morphological, chemical properties, and electronic transport properties under the influence of post-annealing treatment. It was observed that the ideality factor has decreased as a function of post-annealing treatment due to the amount of Ni^{3+} concentration. The post-annealing treatment greatly influenced the formation of intrinsic defects of Ni^{2+} states, and it has reduced as a function of increasing annealing temperature, which was confirmed by the XPS analysis. Based on the thermionic emission and Cheung model, barrier height has been increased as increasing the post-annealing process; on the other hand, the ideality factor has reduced. The interface between the NiO/Al conduction mechanism and barrier inhomogeneity was explained by power law characteristics.

Moreover, grains and grain boundaries of the NiO films greatly contribute to the dielectric permittivity at various frequency regions. Impedance data analysis has shown that the observed behaviour is well fitted with the equivalent electrical circuit.

Acknowledgements

Author contributions

All authors have contributed to the investigation and design. Thin film preparation, device characterisation, and the first draft of the manuscript were realised by PS. All authors have read and approved the final version of the uploaded manuscript.

Funding

Data availability

The data used in the present investigation will be made available on request.

Declarations

Conflict of interest The authors have no relevant financial or non-financial interests to disclose.

References

1. H. Sato, T. Minami, S. Takata, T. Yamada, Thin Solid Films **236**, 27 (1993)
2. X. Zhao, J. Chen, N. Park, Solar RRL **3**, 1800339 (2019)
3. Dhananjay, C.-W. Chu, C.-W. Ou, M.-C. Wu, Z.-Y. Ho, K.-C. Ho, S.-W. Lee, Appl. Phys. Lett. **92**, 232103 (2008)
4. P. Bhat, P. Salunkhe, M.S. Murari, D. Kekuda, Physica B **628**, 413571 (2022)
5. K.H.L. Zhang, K. Xi, M.G. Blamire, R.G. Egdell, J. Phys. **28**, 383002 (2016)
6. Z. Wang, P.K. Nayak, J.A. Caraveo-Frescas, H.N. Alshareef, Adv. Mater. **28**, 3831 (2016)
7. Dhananjay, S.-S. Cheng, C.-Y. Yang, C.-W. Ou, Y.-C. Chuang, M. C. Wu, and C.-W. Chu, J. Phys. D **41**, 092006 (2008).
8. J. You, L. Meng, T.B. Song, T.F. Guo, W.H. Chang, Z. Hong, H. Chen, H. Zhou, Q. Chen, Y. Liu, N. De Marco, Y. Yang, Nat. Nanotechnol. **11**, 75 (2016).
9. R. Touati, I. Trabelsi, M. B. Rabeh, M. Kanzari, J. Mater. Sci. **28**, 5315 (2017).
10. N.A. Al-Ahmadi, Mater. Res. Express **7**, 032001 (2020).
11. S. Nandy, B. Saha, M.K. Mitra, K.K. Chattopadhyay, J. Mater. Sci. **42**, 5766 (2007)
12. A.A. Al-Ghamdi, M.S. Abdel-Wahab, A.A. Farghali, P.M.Z. Hasan, Mater. Res. Bull. **75**, 71 (2016)
13. R. Deng, B. Yao, Y.F. Li, Y.M. Zhao, B.H. Li, C.X. Shan, Z.Z. Zhang, D.X. Zhao, J.Y. Zhang, D.Z. Shen, X.W. Fan, Appl. Phys. Lett. **94**, 022108 (2009)

14. A. Liu, H. Zhu, Z. Guo, Y. Meng, G. Liu, E. Fortunato, R. Martins, F. Shan, Adv. Mater. **29**, 1701599 (2017)

15. M. Stamataki, D. Tsamakis, N. Brilis, I. Fasaki, A. Giannoudakos, M. Kompitsas, Physica Status Solidi (A) **205**, 2064 (2008)

16. P. Salunkhe, M.A. AV, and D. Kekuda, Mater. Res. Express **7**, 016427 (2020).

17. Y.J. Lin, J. Luo, H.C. Hung, Appl. Phys. Lett. **102**, 193511 (2013)

18. H.-L. Chang, T.C. Lu, H.C. Kuo, S.C. Wang, J. Appl. Phys. **100**, 124503 (2006)

19. B. Saha, K. Sarkar, A. Bera, K. Deb, R. Thapa, Appl. Surf. Sci. **418**, 328 (2017)

20. A. Liu, Y. Meng, H. Zhu, Y.-Y. Noh, G. Liu, F. Shan, ACS Appl. Mater. Interfaces. **10**, 25841 (2018)

21. O. Tuna, Y. Selamet, G. Aygun, L. Ozyuzer, J. Phys. D **43**, 055402 (2010)

22. D. Nath, F. Singh, R. Das, Mater. Chem. Phys. **239**, 122021 (2020)

23. H.-L. Chen, Y.-S. Yang, Thin Solid Films **516**, 5590 (2008)

24. P. Salunkhe, M.A. Muhammed, D. Kekuda, Appl. Phys. A **127**, 390 (2021)

25. N. Pant, M. Yanagida, Y. Shirai, K. Miyano, Appl. Phys. Express **13**, 025505 (2020)

26. D.S. Kim, H.C. Lee, J. Appl. Phys. **112**, 034504 (2012)

27. M.W. Roberts, R.S.C. Smart, J. Chem. Soc. Faraday Trans. **1**(80), 2957 (1984)

28. U. Parihar, J. Ray, C.J. Panchal, N. Padha, Appl. Phys. A **122**, 568 (2016)

29. S. Mao, T. Shang, B. Park, D.D. Anderson, S. J. Dillon **104**, 153105 (2014)

30. F. Yakuphanoglu, N. Tugluoglu, S. Karadeniz, Physica B **392**, 188 (2007)

31. Ç. Bilkan, S. Zeyrek, S.E. San, Ş Altındal, Mater. Sci. Semicond. Process. **32**, 137 (2015)

32. D.G. Georgiadou, J. Semple, A.A. Sagade, H. Forstén, P. Rantakari, Y.H. Lin, F. Alkhalil, A. Seitkhan, K. Loganathan, H. Faber, T.D. Anthopoulos, Nat. Electron. **3**, 718 (2020)

33. P. Yang, L. Li, S. Yu, H. Zheng, W. Peng, Appl. Surf. Sci. **493**, 396 (2019)

34. S. Sagar, N. Mohammadian, S. Park, L.A. Majewski, B.C. Das, Nanotechnology **31**, 255705 (2020)